Tellus (1998), 50A, 596–615
Printed in UK – all rights reserved

TELLUS
ISSN 0280–6495

Error growth and Kalman filtering within an idealized baroclinic flow

By CLAUDE FISCHER*, ALAIN JOLY and FRANÇOIS LALAURETTE, *Météo-France, CNRM/GMAP, 42, avenue Gustave Coriolis, 31057 Toulouse Cedex, France*

(Manuscript received 18 July 1997; in final form 8 June 1998)

ABSTRACT

The dynamics of covariances within a baroclinic flow are presented, as obtained by an explicit computation of the forecast error covariance matrix. This is possible since the numerical model is a low-dimensional, semi-geostrophic, uniform potential vorticity model. In addition, idealized observations and observation errors are assimilated with a Kalman filter. This allows for designing a large set of *idealized* observation system simulations (IOSS) where the impact of extra measurements in data sparse areas is studied. The results show that maximal error growth is concentrated along the large-scale frontal strips. When baroclinic interactions are switched off, error growth is enhanced in the upstream parts of the system, and damped in the downstream regions. This shows that barotropic growth alone significantly departs from the mixed barotropic-baroclinic case, so that the baroclinic effects cannot be neglected. The IOSS indicate that a permanent data supply produces a significant damping of error growth, because the data are injected continuously in time. The sensitivity studies show that the positions of the pseudo-observations must be in the vicinity of the frontal structures, and that both the surface front and the tropopause jet have to be sampled. When a widespread, non-permanent observation network is considered, objective targeting strategies are worked out, and their impact on the 2-day forecast error field is studied. The striking feature is the strong dependency of the forecast error on the initial error covariance. It is found that the errors are decreased efficiently by targeted pseudo-observations only if dynamically reshaped correlations are specified, instead of the conventional isotropic ones.

1. Introduction

The purpose of this work is to shed some light on the design of an observing system, suitable for mid-latitude weather prediction. It notably addresses some aspects of cost issues and targeting strategies. The study is carried out with reference to the recent breakthroughs in dynamical meteorology. In particular, Farrell (1988) introduced the concept of singular vectors to describe linear modes that are capable of a strong amplification over a prescribed, finite time. At the validating time, any model solution Φ has an amplification α measured with the use of an inner product in the space of the model solutions:

$$\alpha = \frac{\langle \Phi, \Phi \rangle}{\langle \Phi_0, \Phi_0 \rangle}. \tag{1}$$

The subscript $_0$ denotes initial values. In a linear framework, the model state is evolving with a linear tendency equation: $\Phi = L\Phi_0$, where L is the resolvent system (Joly and Thorpe, 1991). Defining L^* as the adjoint of L with respect to $\langle .,. \rangle$ leads to the following formulation for α:

$$\alpha = \frac{\langle L^* L\Phi_0, \Phi_0 \rangle}{\langle \Phi_0, \Phi_0 \rangle}. \tag{2}$$

The singular modes are defined as the eigenvectors

* Corresponding author.

associated with the operator L^*L. The dominating singular vector is attached to the largest eigenvalues of L^*L and corresponds exactly to the structure that maximizes the quadratic quantity defined in (1). On the whole, singular modes provide a computable set of structures for the study of error growth.

The existence of growing (linear) structures in the atmosphere was long recognized to cause not only extratropical cyclone developments, but also the reduction of predictability at medium-range forecasts (Eady, 1949). Especially, the large potential for amplification of singular modes can provide a significant part of the error growth (Farrell, 1990). Therefore, the singular vector approach is retained in this paper.

Furthermore, the present trend in data assimilation is towards variational techniques such as 3D-VAR and 4D-VAR. In this context, the Kalman filter provides a generalization of the conventional optimal interpolation (OI) schemes, which is formally equivalent to the 4D-VAR approach for a linear model (Ménard and Daley, 1996). Preliminary results are often given for a barotropic model (Bouttier, 1993; Gauthier et al., 1993). In this paper, we show that the barotropic framework might however not be a good approximation since baroclinic features also significantly control the error growth.

To tackle the problem of error growth within a baroclinic flow, we use a Kalman filter type of approach. The filter is implemented in one of the simplest conceptual models that supports baroclinic wave development, namely the uniform potential vorticity model. The latter assumption allows for handling fairly small dimensional state vectors, which makes the complete calculations required in the filter tractable. The model is implemented with the semi-geostrophic (SG) set of equations. We study a generic type of situation, which corresponds to a risk of frontal wave development. We deliberately restrict ourselves to the study of the growth of quadratic errors to gain further in generality. The specific problem of the initial conditions on the error field is included in the problem. Having set the numerical tools for our study, we define so-called Idealized Observation System Simulations (IOSS). Two approaches are retained:

- a fixed network with a few permanent sources of data;
- a set of mobile data sources, that provide non-permanent, widespread information.

In the second case, we test targeting strategies (see Section 5 for an extended presentation), with several sensitivity tests that show both the potential power and the possible restrictions of an objective targeting approach.

In Subsection 2.1, we present the numerical model. Subsection 2.2 is devoted to the implementation of the Kalman filter in the model. Throughout the paper, the same 4D basic state is used as a paradigm of a developing large scale baroclinic system. This flow defines the trajectory along which the linear and adjoint models are integrated. It is presented in Subsection 3.1. The pure dynamics of covariances are discussed in Subsection 3.2. They show how the root mean square (RMS) error on potential temperature (σ_θ) evolves under the influence of the large scale frontal development. The introduction of observations and their analysis is the topic of both Sections 4 and 5. In Section 4, we study the impact of fixed, permanent data sources. The reference case, which is displayed graphically, is one with two sources located at the surface and tropopause fronts, respectively. In Section 5, we tackle the problem of widespread, non-permanent data sources. We discuss the choice and the consequences of an objective targeting approach. Also, some significant discrepancies depending on the initial conditions on covariances are highlighted. A concluding discussion follows in Section 6.

2. Numerical tools

2.1. *The semi-geostrophic model*

The numerical model is based on the adiabatic, semi-geostrophic (SG) equations (Hoskins (1975) as implemented by Joly (1995)). In particular, potential vorticity is taken to be uniform and steady in the domain interior, so that the dynamics are driven by the potential temperature anomalies at the lower and upper boundaries. A cartesian geometry on an f-plane is used. The flow is contained in a periodic channel (Y-direction) between two lateral walls (X-direction). Solid lids are located at the surface $Z=0$ and at the so-called tropopause $Z=H$, where Z is the vertical pressure-coordinate introduced by Hoskins and

Bretherton (1972). In the following, we take $H = 8000$ m. Furthermore, no horizontal diffusion is used.

The SG system allows for a closer study of frontogenetical phenomena, since the SG equations hold closer to the frontal collapse than the quasi-geostrophic equations (Hoskins, 1975). The main feed-back between the thermal gradients and the ageostrophic flow is made implicit in the coordinate change:

$$X = x + \frac{v_g(x, y, z)}{f}, \qquad Y = y - \frac{u_g(x, y, z)}{f}, \qquad Z = z, \tag{3}$$

where u_g and v_g stand for the components of the geostrophic wind. The space change is possible as long as the jacobian of the transformation remains strictly positive everywhere:

$$J_X = \frac{\partial(X, Y)}{\partial(x, y)} = \left\{1 - \frac{1}{f}\left(\frac{\partial V_g}{\partial X} - \frac{\partial U_g}{\partial Y}\right) + \frac{1}{f^2}\frac{\partial(U_g, V_g)}{\partial(X, Y)}\right\}^{-1} > 0. \tag{4}$$

In the following, variables in physical space are in lower case letters, while variables in the geostrophic space are in upper case ones. In particular, the tendency equation for the potential temperature field at each boundary reads:

$$\frac{\partial \delta\Theta}{\partial t} = -\delta U_g \frac{\partial \delta\Theta}{\partial X} - \delta V_g \frac{\partial \delta\Theta}{\partial Y} - \left[\frac{\partial \Theta}{\partial X}\right]\delta U_g - \langle V_g \rangle(X, Z)\frac{\partial \delta\Theta}{\partial Y}, \tag{5}$$

with $\langle V_g \rangle(X, Z)$ the steady zonal large scale component of the geostrophic wind. For our experimental needs, the numerical tools include the direct, nonlinear model, the tangent linear version, as well as its adjoint. The latter two are essential for the development of a Kalman filter. Note also that the assumption of uniform potential vorticity forces very simple, two-dimensional vertical structures, so that the state vector reduces to a limited, truncated set of coefficients. Also, maximal amplitude is always achieved at the boundaries.

2.2. *The Kalman filter*

The Kalman filter was first used to control error growth on experimental noise (Kalman, 1960, Kalman and Bucy, 1961). Within atmospheric data assimilation, it allows for fitting sequentially the model state to the observations, at each observation time. The analyzed field then corresponds to the state of minimum mean square error, weighted by the prescribed covariances. An important aspect of the Kalman filter is that it takes into account the time evolution of the system. Thus, the variance-covariance matrix itself is time dependent (see below). In that sense, the Kalman filter is mathematically equivalent to the four-dimensional variational assimilation, with the difference that the latter does not provide the explicit expression of the foreward integrated covariance matrix. In contrast, the standard analysis techniques in operational numerical weather prediction use optimal interpolation (Gandin, 1963; Rutherford, 1972), with a fixed, steady, variance-covariance matrix.

The Kalman filter is introduced in atmosphere-ocean data assimilation by Ghil et al. (1981) for a linear shallow water model. It is generalized to a nonlinear shallow water model by Budgell (1986) and to a global barotropic model by Gauthier et al. (1993). The filter is implemented in the SG model in the following way (subscript k denotes the time step, superscripts f and a stand for the forecast guess and the analysis, respectively).

1. Nonlinear time integration from time t_k to t_{k+1}:

$$Z^f_{k+1} = M(Z^a_k); \tag{6}$$

M represents the nonlinear model and Z the state vector.

2. Linear time integration of the analyzed error covariances available at time t_k:

$$P^f_{k+1} = L P^a_k L^*. \tag{7}$$

L represents the tangent model, integrated between t_k and t_{k+1} (also called the resolvent system) and L^* its adjoint. Definitions and simple examples of a resolvent system L are shown in Joly and Thorpe (1991) and Fischer (1998). P is the error covariance matrix for the spectral coefficients. Three points are to be stressed.

- The resolvent L contains the information on the linear dynamics that govern the flow: amplifying modal structures, growth rates, phase speeds.

Thus, the forecast covariances are consistent with the dynamics of the flow and exhibit also modal structures (see Fischer, 1998). This is the crucial difference to the operational OI techniques, where isotropic and homogeneous error fields are assumed.

- The choice of the initial covariances remains open. This problem is addressed in Sections 4 and 5.

The model is assumed to be perfect, so that forecast errors only come from the initial errors (matrix P_0), and from the uncertainty of the pseudo-observations (matrix R_k below). Moreover, the model errors are not introduced in our study.

3. The analysis step:

$$G_{k+1} = P^f_{k+1} H^t_{k+1} (R_{k+1} + H_{k+1} P^f_{k+1} H^t_{k+1})^{-1}, \tag{8}$$

$$P^a_{k+1} = (I - G_{k+1} H_{k+1}) P^f_{k+1} \tag{9}$$

$$Z^a_{k+1} = Z^f_{k+1} + G_{k+1}(X_{k+1} - H_{k+1} Z^f_{k+1}) \tag{10}$$

G_{k+1} is the gain matrix, H_{k+1} is a linear interpolator from the state vector to the observations, the superscript t denotes the transposition. R_{k+1} is the error variance matrix of the observations, I stands for the identity matrix and X_{k+1} is a vector that contains the observed fields. Note that a linear interpolator is used here, instead of a complete, nonlinear one as in Gauthier et al. (1993). Furthermore, the uncertainty on the coordinate change from geostrophic to physical space is neglected (Bernardet, personal communication, and Fischer, 1997). This neglect results in an underestimation of the physical space error variances, which is addressed in Section 5 and in Appendix A. Only observation error variances are considered: the observations are assumed to be uncorrelated, so that R_{k+1} reduces to a diagonal matrix.

The gain matrix G_{k+1} is defined so that the analyzed mean square error is minimized. The proof of its formulation may be found in Ghil (1989) or Fischer (1997), Appendix C. Note also that the analysis step can be split into two parts.

- The analysis of the error covariance matrix which leads to P^a_{k+1} (eq. (9)).
- The analysis of the state vector which leads to Z^a_{k+1} (eq. (10)).

The second step can be considered as the most interesting one in operational data assimilation, since it provides the initial field for the next forecast. Anyway, in this study, we are only concerned with error growth, without actually correcting the model state itself. Therefore, this paper presents the results obtained by analyzing the covariance matrix alone. This is equivalent to having observations that always confirm the forecast. However, due to the uncertainty on the observations, this forecast receives new, lower, error statistics.

The assumption of taking the same model for control and assimilation, a technique referred to as an "identical twin approach", is valid in our idealized framework, as far as the observations are chosen consistently with the simplified dynamics and no difference in resolution is used between forecast and analysis. On the contrary, in real atmosphere assimilation systems, the identical twin approach is limited by the model errors, which are then an extra source of errors whose neglect can cause the Kalman filter to diverge. Model errors would require a more sophisticated filtering approach, such as an adaptive filter (Dee, 1995) or a Kalman smoother (Ménard and Daley, 1996).

If N is the dimension of the spectral state vector, then the Kalman filter uses square matrices of dimension N^2. In operational models, $N \approx 10^5$, so that matrices like P^a_k or P^f_k cannot be handled with the present generation of computers. Since the SG model has a strong balance condition, its state vector is much smaller (typically, $N \approx 500$). This allows for a complete computation of the time integration of the covariance matrix, and provides results that are not subject to any simplification on that matrix. This is one of the strength of the present work.

3. Dynamical error growth

3.1. The trajectory

In the subsequent results, the same trajectory is employed: it is made up of two parts. First, a steady, large-scale zonal jet forms a suitable background. Second, an evolving baroclinic eddy is included as well. It is initially obtained as the singular mode that maximizes enstrophy within the box Ω (Fig. 1), over 2 days. The solution propagates and develops as a wave train along the zonal jet. As an example, Fig. 1a,b show the potential temperature field at day 6 at 0 and 8000 m. This pattern is the result of the nonlinear

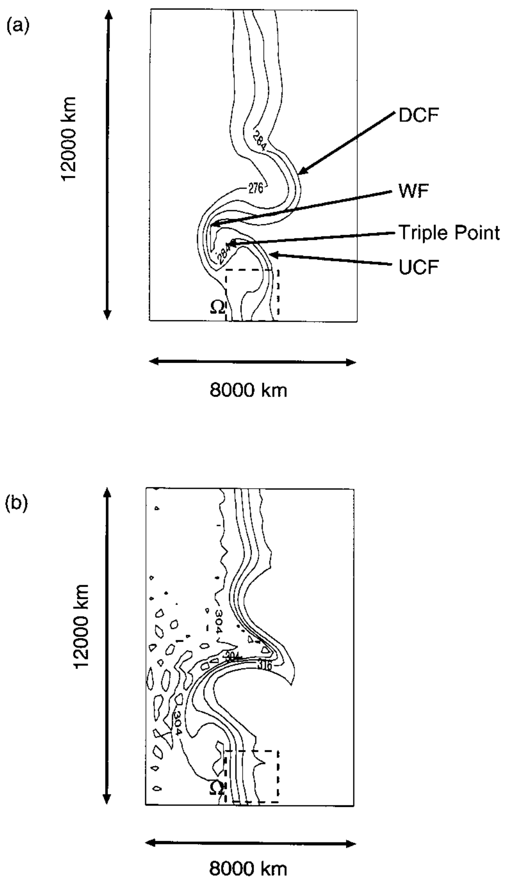

Fig. 1. Potential temperature θ every 4 K for the trajectory, after 6 days in the nonlinear model. (a) 0 m, (b) 8000 m.

integration. The upper thermal wave is in advance, compared to the surface thermal wave, which is characteristic of baroclinic wave development. Three frontal areas are distinguished:

- a downstream cold front (DCF on Fig. 1a);
- a warm front in the medium part (WF);
- an upstream cold front (UCF).

Furthermore, in the foremost part of the so-called occlusion, at the junction between WF and UCF, we define a "triple-point" (Fig. 1a). Thus, this system is chosen to be representative of the formation of a long trailing front in the wake of a large-scale baroclinic wave.

The trajectory chosen in this study consists of the non-linear evolution of this large-scale wave between day 6 and day 8. For the study of error covariances, the linear integrations are performed along that 48-h trajectory. Fig. 2 shows the potential temperature field at day 8, at 0 and 8000 m. The wave has propagated downstream with a group velocity of about $v_{\text{group}} \approx 8.3\ \text{m s}^{-1}$. The frontal gradients are increased, when compared to Fig. 1. Frontogenesis is still underway, so that the wave exhibits a clear nonlinear structure at day 8.

At day 6, and at 0 m, the values of the jacobian J_X are of about 3.5 in the rear part of WF. At 8000 m, maxima reach locally 8, with an overall value of about 4 in the frontal strip (not shown). At day 8, maxima reach locally 4 and 10 in WF at 0 m, and 10.5 at 8000 m. Otherwise, values of about 2 are observed along the surface front (DCF and UCF), while the jacobian exceeds 4 at the tropopause front. These values show that the

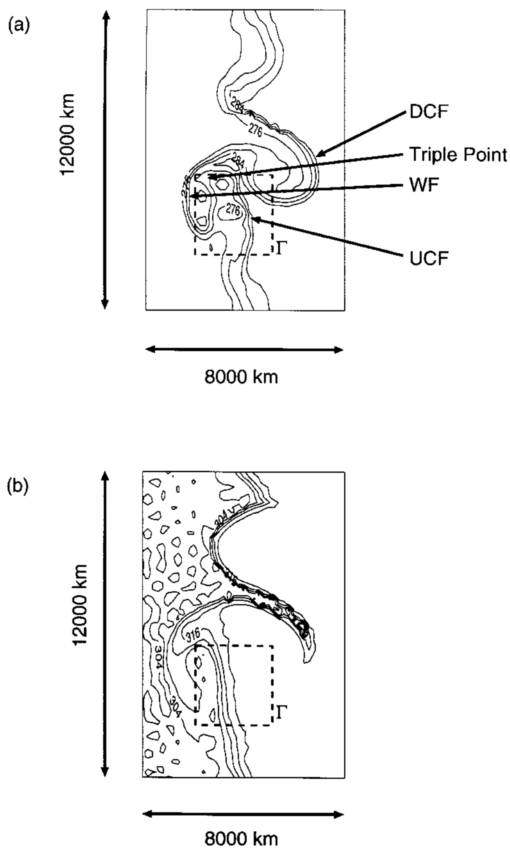

Fig. 2. Potential temperature θ every 4 K for the trajectory, after 8 days in the nonlinear model. (a) 0 m, (b) 8000 m.

frontal structures are fairly strong and the trajectory is not taken further than day 8, to avoid numerical inconsistencies due to too large jacobians.

For the numerical parameters, we run the models with 40 points in the X direction (which means a resolution of 200 km). This is a compromise which allows for catching the overall baroclinic structure and keeping a small enough state vector to handle the large error covariance matrix. Anyway, we do not aim at simulating subsynoptic structures in this work. The time step is 900 s and we recall that the model runs without viscosity.

3.2. *Error growth driven by pure dynamics*

The Kalman filter, as introduced in Subsection 2.2, consists in a linear forecast (eq. (7)) and an analysis of the error covariance matrix (eq. (9)). If no analysis is performed between t_0 and t_k, then the final error covariances simply result from a purely dynamical growth of the initial error covariances along the reference trajectory. In the subsequent developments, only error covariances on the potential temperature field $\delta\theta$ are considered, since this is the basic time dependent model variable (see relation (5)). Three different initial error covariances are used (noted C1, C2 and C3):

C1: a uniform and isotropic covariance field is defined. The initial field is defined on geostrophic space potential temperature, by the relation:

$$\mathrm{cov}_\theta(i, j) = \sigma_0(Z_i)\sigma_0(Z_j)\, \mathrm{e}^{-D_{ij}^2/a^2}\, \mathrm{e}^{-Z_{ij}^2/b^2}, \qquad (11)$$

which gives the covariance between points i and j, separated by a horizontal distance D_{ij} and a vertical distance Z_{ij}. a and b are two characteristic ranges, taken to be 500 km and 5000 m, respectively. σ_0 is a horizontally uniform root mean square error (RMS), equal to 1 K at the surface and 2 K at the tropopause (in sensitivity tests, also 2 K and 4 K, respectively). These magnitudes are suggested by operational results.

C2: a dynamically reshaped covariance field is computed. This field is obtained by integrating the previous initial covariances along the trajectory, from day 5 + 1/2 to day 6. Thus, the "initial" covariances at day 6 have the shape of an error field after a 12 h evolution with equation (7). Note that, due to the 12 h integration, the RMS values are enhanced, so that at day 6 we get about 2 K at 0 m and 3.2 K at 8000 m, in the frontal strips, for initial 1 K and 2 K.

C3: the dynamically reshaped covariances are renormalized at day 6 to their true initial RMS values (1 K at 0 m and 2 K at 8000 m, or 2 K and 4 K, respectively). This gives a covariance field with uniform variances, but with still flow dependent error correlations.

3.2.1. Mixed baroclinic-barotropic error growth. Fig. 3a, b show the potential temperature RMS

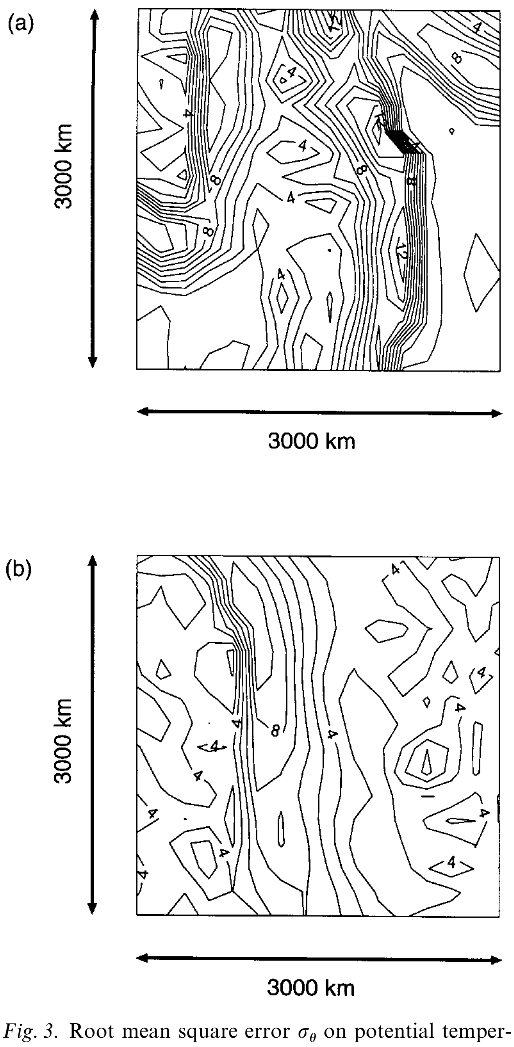

Fig. 3. Root mean square error σ_θ on potential temperature at day 8, every 1 K (48 h linear integration). (a) 0 m, (b) 8000 m. The field is displayed in the subdomain Γ defined on Fig. 2.

error σ_θ for day 8. Initial variances at day 6 are uniform (condition C1 with σ_θ set to 1 K at the surface and 2 K at the tropopause). We display the fields in the subdomain Γ defined on Fig. 2. This area covers most of the upstream cold front, in the rear part of the main baroclinic system. This is the domain on which we focus the IOSS and the study of error prediction. It is seen that the 48-h linear integration results in enhanced RMS errors along the frontal strips. The σ_θ-values vary from 6 to 13 K at the surface. Outside the frontal band, the values are rather uniform, at about 4 K. At the tropopause, σ_θ is changed from 2 K initially to about 4 K, with larger values up to 9 K in the frontal area.

Thus, the errors increase quickly in the active frontal areas, where strong gradients are generated and linear modes are capable of amplification. From a dynamical point of view, error growth is achieved where a potential for linear amplification exists. From a statistical point of view, errors are largest in those areas where the potential temperature field is the most varying. Therefore, σ_θ is enhanced in the frontal bands, where it measures the uncertainty on the intensity and the location of the frontal gradient. On the contrary, σ_θ remains smaller outside of the frontal strips, where the fields are uniform.

Note also that σ_θ grows quicker at the surface than at the tropopause. This shows that the surface modes have larger growth rates than the tropopause modes.

For a second case, the initial non-uniform non-isotropic variances-covariances C2 are integrated over the 48-h period. At day 8, the σ_θ values have the same shape than on Fig. 3, but they are larger (maximum of 17 K at the surface, and 12 K at 8000 m). Finally, if the non-uniform variances at day 6 are renormalized to their true initial values (1 K at 0 m, 2 K at 8000 m, condition C3), then the 48 h integrated σ_θ is close to the case C1 with isotropic covariances. However, the maxima are somewhat larger, which is due to the fact that the covariances are fitted to the flow as a result of the first 12-h integration. Thus, they project onto linear structures that amplify afterwards more efficiently than the isotropic structures.

3.3.2. Pseudo-barotropic error growth. It is possible, in the context of the code employed in the present study, to restrict the tangent linear model to a pseudo-barotropic one. The non-linear trajectory, however, is the same one. This is achieved by taking a very small height H for the top lid in the linear model. Indeed, the scales for baroclinic interactions are those that verify $k^{-1} \leqslant L_R$, with k the horizontal wavenumber and $L_R = NH/f$ the Rossby radius of deformation. When $H \to 0$, the baroclinic scales are no longer supported by the truncated wave representation. The pseudo-barotropic version of the model has been validated by the computation of Rayleigh-like modal instability characteristics (not shown).

Fig. 4 shows σ_θ at day 8, starting with the uniform, isotropic field. This field must be compared to Fig. 3a, which corresponds to mixed baroclinic–barotropic development. The pseudo-barotropic values are smaller by almost 2 K in the DCF (not shown). On the other hand, the pseudo-barotropic σ_θ is larger than in the mixed case in the rear part of the WF and around the triple point, as well as in the UCF. In the vicinity of the triple point, σ_θ values are increased by about 2 (locally 5) K; in the UCF band, we have an overall increase of 2 (locally 3) K.

Thus, in the pseudo-barotropic regime, surface errors grow quicker in the trailing part of the large scale system (so-called triple point and UCF). Compared to the complete, mixed case

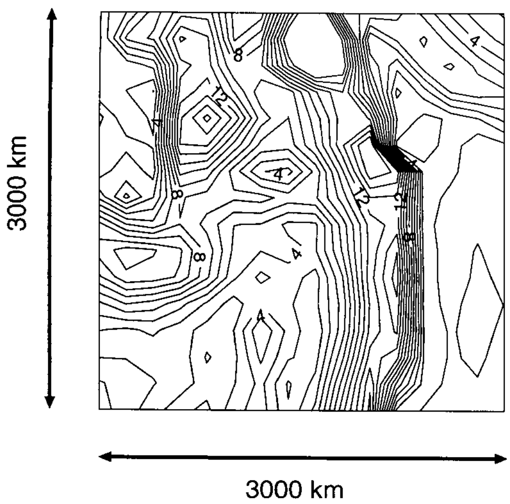

Fig. 4. Root mean square error σ_θ on potential temperature at day 8, every 1 K (48 h linear integration) in the pseudo-barotropic experiment. The field is at 0 m, and in the subdomain Γ defined on Fig. 2.

($H = 8000$ m), the baroclinic modes are now missing. Therefore, the surface trapped barotropic waves cannot interact with the baroclinic modes, and the error variance is not redistributed between the two standard model levels $Z = 0$ and $Z = H$. From a dynamical point of view, it is seen that the isotropic correlations project better on the pseudo-barotropic optimal modes than on the mixed ones. Note that our result also holds for the dynamically fitted correlations (C2). In this latter case, the extra increase in the 48 h RMS error is of about 2–3 K in the pseudo-barotropic run.

Alternatively, in a statistical-type of approach, one can say that, when baroclinic interactions are possible, then the surface level (say) feels part of the information stored at the tropopause level. The dynamical signature of this exchange of information is simply provided by the classical Rossby-wave interaction. Thus, each level has a damping effect on the error growth at the other level. When the vertical interactions are switched off, the pseudo-barotropic errors grow without this damping since the level of interest is nomore forced by the input of information from the companion level. Thus, barotropic modes are increasing efficiently the 48 h RMS error forecasts, while the baroclinic modes have rather an attenuating effect. This is one important conclusion of this study. Results of error growth based on barotropic models (Bouttier, 1993) are overpessimistic, given that the midlatitude flow is predominantly baroclinic. On the other hand, in the DCF part of the large scale structure, baroclinic development is probably more important, since its missing makes the RMS values decrease.

4. Impact of a fixed and permanent source of data

This section deals with IOSS that use a fixed source of data, such as data that are provided by ships. The pseudo-observations are obtained at a few constant locations in space, but with a regular spacing in time. In this sense, the experimental design sketches a conventional, ground-based, observation network. We recall that the IOSS actually only concern the analysis of the error covariance matrix, without modifying the model trajectory itself (eq. (9)). The experiments are implemented by defining the space and time range of the fixed source of data.

- Each observation is equivalent to a sounding in the model atmosphere. It consists of one observed value at the surface ($Z = 0$) and another one at the tropopause ($Z = H$). This is consistent with the fact that the model only has two independent levels on Z. More than two values can be chosen on one sounding, but this can result in numerical singularities due to the linear dependencies. Alternatively, a vertical error correlation matrix is needed to reduce the actual number of degrees of freedom, which is contrary to many real observation types.
- The location of each pseudo-observation point is kept constant throughout the IOSS.
- The soundings are performed every 6 h, between day 6 (start time for the IOSS) and day 8 in the singular mode's life cycle presented in Subsection 3.1. Thus, OI is performed with a 6-hourly frequency and there are 9 analysis steps on the whole.

Observation RMS errors are constant and, for potential temperature, we choose that constant to be $\omega = 1$ K, again inspired by operational orders of magnitude.

Figs. 5a,b show the RMS values σ_θ, at day 8. Two sources of data are located in the UCF: one on the surface front, the other below the tropopause front. For the case of Fig. 5, the initial variances-covariances are uniform and isotropic (condition C1).

The impact of the data is obtained by comparison with the pure dynamical growth cases. Several points are to be stressed.

- The maxima for σ_θ are about 7 K at the surface and 6 K at the tropopause. This means a 50% reduction at day 8, compared to pure dynamics, inside the frontal areas.
- The impact of the data is significant up to 2000–2500 km downstream of the source locations. This is due both to the advection of low σ_θ by the basic state flow and to the propagation through the linear model of low-σ_θ modes by projection onto amplifying or propagating modes.
- The impact is greatest in their vicinity. This comes from the continuity properties of all the operators involved in the error computation (resolvent L, Fourier transforms, geostrophic coordinate transform).

In addition to this reference IOSS, with two

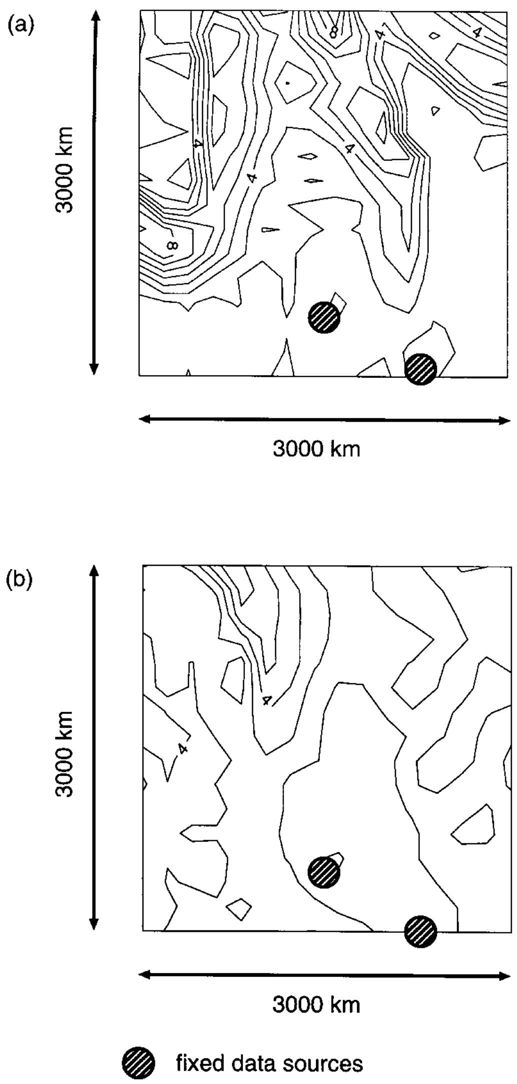

Fig. 5. Root mean square error σ_θ on potential temperature at day 8, every 1 K, for the case of two fixed and permanent data sources that provide an analysis step every 6 h. (a) 0 m (b) 8000 m. Initial variances are uniform, and covariances are isotropic. The field is displayed in the subdomain Γ defined in Fig. 2.

sources, we show the results of a number of sensitivity experiments. The results are displayed in Table 1. Three cases are distinguished, depending on the initial covariance matrix: a first set of IOSS is performed with uniform variances at day 6 (condition C1), a second set uses the dynamically reshaped covariances (condition C2) and the 3rd set consists in two cases for which the dynamically reshaped covariances have renormalized variances (condition C3). We change the locations (and number) of the data sources, in order to measure the sensitivity to their positions with respect to the frontal strips. The values of σ_θ in Table 1 consist in a minimum and a maximum, as noted for each case inside the UCF band and the Γ-domain. The relative reduction in σ_θ is measured by comparison with the pure dynamics case, for each of the three initial covariance fields. Note that the case "surface+tropopause (2)" corresponds to Figs. 5a,b with initial uniform variances. The case "none" corresponds to Figs. 3a,b with initial uniform variances (pure dynamics).

The following results are emphasized.

- As expected, the largest σ_θ values are obtained in the pure dynamics case. The smallest values are noticed for the case with two sources and 6 hourly analysis steps all over the 48-h period. All other IOSS are less efficient in reducing σ_θ. This is either due to the fact that they are less rich in information (fewer observations), or due to the bad locations of the data sources, away of the frontal structures.
- If only one source is retained, then the reduction in σ_θ is strongest in the vicinity of the corresponding front. Thus, if the source on the surface front is retained, then the RMS reduction is efficient at the surface front, and close to the case with the two sources. On the contrary, values at the tropopause are larger. Also, if the source below the tropopause front is retained, then the RMS reduction is efficient at the upper front, but the values at the surface front are increased. Thus, the position of a unique data source has a significant impact on the location of the largest error reduction.
- When the two sources are away from the frontal strips, the RMS reduction is quite low: 10% with initial uniform variances C1 and 20% with initial non-uniform variances C2.
- If the analysis cycle is broken up at day 7 (so that the last 24 h are controlled by pure dynamics), then the RMS reduction is reduced compared to a complete 48-h analysis cycle. The relative reductions are quite similar to the cases with only one source, over the 48-h period. This shows that it is important to perform the analysis cycle as close as possible to the validating time.
- The experiments with initially non-uniform

Table 1. *Summary of the several IOSS that use fixed, permanent observations*

Locations (number)	No. soundings	Root mean square error σ_θ of $\delta\theta$ in K at day 8		$\frac{\lvert \mathrm{Max}(\sigma_\theta) - \mathrm{Max}(\sigma_{\theta\mathrm{ref}}) \rvert}{\mathrm{Max}(\sigma_{\theta\mathrm{ref}})}$	
		surface	tropopause	surface	tropopause
Initial uniform variances and isotropic covariances					
none (reference)	0	6–13	4–9	0	0
surface + tropopause (2)	18	2–7	3–6	46%	33%
surface (1)	9	4–8	4–7	38%	22%
tropopause (1)	9	5–9	3–6	30%	33%
away from fronts (2)	18	5–12	4–8	7%	11%
surf + tropo, over 24 h (2)	10	3–9	4–7	30%	22%
Initial non-uniform variances and non-isotropic covariances					
none (reference)	0	6–17	5–12	0	0
surface + tropopause (2)	18	2–8	2–7	53%	42%
surface (1)	9	2–9	3–8	47%	33%
tropopause (1)	9	3–10	2–7	41%	42%
away from fronts (2)	18	5–14	5–10	18%	17%
surf + tropo, over 24 h (2)	10	3–10	4–8	41%	33%
Initial renormalized variances and non-isotropic covariances					
none (reference)	0	6–15	5–11	0	0
surface + tropopause (2)	18	2–7	3–6	53%	45%

Each experiment is defined by the locations of the data source(s) with respect to the surface and tropopause fronts. The total number of sources is indicated in parentheses.

variances (C2) confirm the results with initially uniform variances (C1). This shows that the IOSS provide very good results, whatever the initial covariance field is. Fixed and permanent data allow for a robust and significant reduction in σ_θ. Note simply that the relative reduction is somewhat larger with non-uniform variances, because these variances are larger at day 6. This is also the case when the variances are renormalized at day 6, due to the effects of the non-uniform, dynamically reshaped correlations (C3). This demonstrates that the classical, fixed observing network is not very sensitive to the structure of the initial correlations.

5. Impact of a widespread and non-permanent source of data

The alternative to a set of a few permanent data sources is to perform an extensive sampling, typically by employing a mobile vector such as an aircraft. In particular, the possibility of concentrating the measurements in a "target" localised in space and time is examined in this section. Contrary to the previous IOSS, where data are available over the 48-h period, the non-permanent data supply occurs only within a limited time interval. This interval is taken to be from day 6 to day 6 + 3 h. Afterwards, the error covariances again evolve in time through pure dynamics. Having an aircraft type of vector in mind, the locations of observations are changing with time, along prescribed tracks. Thus, a complementary view is obtained: the IOSS of the present section have data that are localized in time and widespread in space while the previous ones have observations that are widespread in time but at fixed spatial locations.

Because the observations are only defined in the first three hours, they have an impact through the modified initial conditions. Indeed, these experiments test how a high-frequency analysis cycle impacts on the covariance field at day 6 + 3 h, and afterwards on the day 8 fields, after a 45-h linear integration. Thus, the analysis cycles are almost equivalent to a modification of the initial covariance matrix, followed by a 45-h dynamical growth. This similarity is also shown by the result in Table 3, where the "one-time-only" case is similar to the "complete targeting" case over three hours.

Note that the observations are defined in the same way as the pseudo-soundings of the previous experiments: except when otherwise stated, they consist of two values, one at the surface and one at the tropopause level. Observation RMS error is fixed to $\omega = 1$ K for σ_θ; the errors are uncorrelated in time and space. Also, the IOSS are repeated with the 3 different initial covariance matrices defined in Subsection 3.2. The sensitivity to the targeting track is investigated and summarized in Table 2. The sensitivity to the observation error variance, as well as to the initial background error variance, is studied and presented in Table 3.

One important aspect is to define the sampling pattern. We are interested again in the error growth in the Γ-domain defined on Fig. 2. A simple pattern is defined as a straight track, upstream of Γ, orthogonally to the frontal structures and along the "western" edge of domain Γ, at $Y = 2000$ km. Observations are taken every 1/2 h, during the 3 h analysis period. It can be seen on Table 2 that the observations have a small impact when initial uniform and isotropic variances-covariances (C1) are used, with a relative reduction of only about 10%. On the other hand, when initial non-uniform, non-isotropic errors (C2) are used, the impact is drastically increased and reduction of about 45% are achieved at both levels.

Another way of defining a suitable pattern is to use an objective criterion. This criterion is obtained by computing the sensitivity function of a prescribed target, a technique commonly refered to as "objective targeting" (Snyder, 1996, Palmer et al., 1998). The first order term in the Taylor expansion of a quadratic function $F(Z) = \langle Z, Z \rangle /2$ (with Z the state vector) reads:

$$\delta F = \langle Z, \delta Z \rangle . \tag{12}$$

Use of the resolvent system L and of its adjoint

Table 2. *Summary of the several IOSS that use non-permanent, widespread data*

Tracks (number)	No. soundings	Root mean square error σ_θ of $\delta\theta$ in K at day 8: surface	tropopause	$\frac{\lvert \mathrm{Max}(\sigma_\theta) - \mathrm{Max}(\sigma_{\theta\mathrm{ref}}) \rvert}{\mathrm{Max}(\sigma_{\theta\mathrm{ref}})}$: surface	tropopause
Initial uniform variances and isotropic covariances					
none (reference)	0	6–13	4–9	0	0
orthogonal transect (1)	7	6–12	4–8	7%	11%
complete targeting (2)	26	6–10	4–7	23%	22%
downstream targeting (2)	13	5–11	4–8	15%	11%
upstream targeting (2)	13	6–11	4–7	15%	22%
limited targeting (2)	26	6–11	4–7	15%	22%
surface targeting (2)	26	6–13	4–9	≈0	≈0
Initial non-uniform variances and non-isotropic covariances					
none (reference)	0	6–17	5–12	0	0
orthogonal transect (1)	7	6–9	5–7	47%	42%
complete targeting (2)	26	5–8	4–5	53%	58%
downstream targeting (2)	13	5–10	4–7	41%	42%
upstream targeting (2)	13	6–12	4–8	29%	33%
limited targeting (2)	26	5–11	5–7	35%	42%
surface targeting (2)	26	6–13	6–9	24%	25%

Each experiment is defined by the track(s) of the mobile source(s). The total number of tracks is indicated in parentheses.

Table 3. *Summary of the several IOSS that use non-permanent, widespread data*

Type of experiment	No. soundings	Root mean square error σ_θ of $\delta\theta$ in K at day 8		$\frac{\lvert \mathrm{Max}(\sigma_\theta) - \mathrm{Max}(\sigma_{\theta\mathrm{ref}}) \rvert}{\mathrm{Max}(\sigma_{\theta\mathrm{ref}})}$	
		surface	tropopause	surface	tropopause
Initial renormalized variances and non-isotropic covariances					
initial $\sigma_\theta = 1$ and 2 K	0	6–15	5–11	0	0
complete targeting (2)	26	5–7	4–5	53%	55%
one-time-only (2)	26	5–8	4–5	46%	55%
obs. RMS $\omega = 2$ K	26	6–10	5–7	33%	36%
obs. RMS $\omega = 0.5$ K	26	4–6	3–4	60%	63%
initial $\sigma_\theta = 2$ and 4 K	0	12–31	14–22	0	0
complete targeting (2)	26	8–13	6–9	58%	59%
Initial uniform variances and isotropic covariances					
initial $\sigma_\theta = 2$ and 4 K	0	12–28	12–19	0	0
complete targeting (2)	26	11–19	8–13	32%	31%

Several sensitivity results are displayed, depending on the time distribution, the initial observation RMS error ($\omega = 1$ K, unless otherwise stated) and the initial background RMS errors (surface/tropopause). The 2 tracks of the mobile sources are those of Fig. 6b, for complete targeting.

L^*, with respect to $\langle .,. \rangle$, leads to:

$$\delta F = \langle L^* Z, \delta Z_0 \rangle = \langle \nabla_0 F, \delta Z_0 \rangle . \tag{13}$$

This relation gives the gradient of F with respect to the initial conditions. Thus, a first possibility to measure the sensitivity of F is to compute the gradient $\nabla_0 F = L^* Z$. This approach is used for example in Bergot et al. (1996) with F the total enstrophy, and in Langland et al. (1996), with F the mean vertical vorticity in a column of air. In these cases, the sensitivity consists in displaying those areas where a unit initial variation δZ_0 (with $\| \delta Z_0 \| = 1$) creates the largest change δF in F. Maps of gradient fields therefore basically indicate where the "potential" sensitivity is largest, without information on where it is most judicious to change the initial conditions Z_0.

As an example, Rabier et al. (1996) choose F to be the total energy. They define the error field at a given validating time (48 h) by the difference between forecast and analysis:

$$\varepsilon = Z^f - Z^a , \tag{14}$$

so that the gradient reads:

$$\nabla_0 F = L^* \varepsilon . \tag{15}$$

The authors are eventually interested in finding a perturbation of the initial conditions that decreases the departure between the forecast and the analysis at validating time. It is shown that the following field:

$$\delta Z_0 = -\frac{1}{\mu_1} \nabla_0 F , \tag{16}$$

with μ_1 the dominating eigenvalue of $L^* L$, allows for a better forecast at further validating times. The authors point out that the discrepancies between forecast and analysis decrease not only at 48 h (which is expected by construction), but also at later validating times, up to 120 h, when the assumption of linear development of the error field does not hold anymore. However, this technique uses the analyzed fields Z^a, which means that this method cannot be employed in advance to the first validating time.

It is possible to go one step further. We introduce an error in the initial field, noticed ε_0. This error is supposed small, compared to the trajectory, so that its time evolution is driven by linear dynamics. Therefore, with the use of the resolvent:

$$\varepsilon = L \varepsilon_0 . \tag{17}$$

We now consider that $\varepsilon = Z$, so that the previous developments allow for expressing the gradient $\nabla_0 F$ as a function of the initial error field:

$$\nabla_0 F = L^* L \varepsilon_0 . \tag{18}$$

This relation shows that the largest gradients are obtained when ε_0 is the dominating eigenvector of the hermitian operator L^*L. This problem is exactly equivalent to finding the first singular mode of L (Joly, 1995, Fischer, 1998). The dominating eigenvector ε_1 can be viewed as the structure of the initial error field that produces the largest departure δF over the prescribed period (Lacarra and Talagrand, 1988). Thus, the singular mode approach gives a different interpretation for the displayed sensitivity field, than the gradient field. Moreover, this method can be applied before validating time, with the resolvent system integrated over the forecast trajectory.

In this paper, we express the sensitivity of the variance of $\delta\theta$ at day 8 with respect to the $\delta\theta$ field at day 6, by using relation (18). The choice of the variance of potential temperature is made because the error field that is studied here is the RMS error σ_θ of $\delta\theta$. We compute the dominating singular mode with respect to potential energy in the Γ'-domain defined on Fig. 6a (note that the background temperature field in Fig. 6a is exactly the same as on Fig. 2a). The resulting field at day 6 is displayed in Figs. 6b, c.

The singular vector has an overall baroclinic shape, with a temperature anomaly at the tropopause that has an opposite sign to the one at the surface. Also, in the linear evolution of the mode (not shown), meridonal fluxes $\delta u_g \delta\theta$ play a significant role in the growth of potential energy inside Γ'. Note that the spatial structures shown on Figs. 6b, c have large extents. Each kernel has a typical surface of about $4000 \times 2000\ \mathrm{km}^2$. The general horizontal shape of the singular vector, with its elongated and rotated patches, is reminiscent of structures observed in other works, such as in Palmer et al. (1998) for the energy-related singular vectors.

We define "complete targeting tracks" as indicated by the 2 thick-dotted broken arrows on Fig. 6b. Note that these paths are chosen to cross the areas of minima and maxima in perturbation temperature ($\delta\theta$), as well as the areas with strong gradients in $\delta\theta$. On the other hand, limited tracks are readily defined by choosing limited-range paths, as shown on Fig. 6c. Mobile data sources are placed every 15 min, during the 3-h analysis period. In addition to these two IOSS, a few variations of the targeting tracks are studied, with modified tracks or only surface observations (see Table 2).

Moreover, we try to assess the impact of having neglected the SG coordinate change in the computation of the error covariances. As shown in Appendix A, this simplification results in an underestimation of the physical space variances and thus, in an overuse of the forecast background in the analysis, at the expense of the observations. However, while the underestimation might become important for wind errors (multiplication of σ_V^2 by J_X^2, with $J_X \in [1, 10]$ in our case), it is less stringent for temperature variance (additional correction of σ_Θ^2 by $k'\sigma_V^2$, the latter term having the same order of magnitude than σ_Θ^2). Therefore, extra sensitivity tests have been performed, by either keeping the observation RMS error $\omega = 1$ K and increasing the initial σ_Θ^2 (by a factor of 4), or modifying $\omega = 0.5$ and 2 K while keeping the reference σ_Θ^2 (Table 3).

The tables give minimum and maximum σ_θ-values in the frontal strips, along with the relative reductions, when compared to the pure dynamics case. For comparison, note that the case "none" in Table 2 corresponds to Fig. 3 with the initial uniform and isotropic errors C1 (pure dynamics). The case "complete targeting (2)" in Table 2 with initial isotropic covariances corresponds to Fig. 7. The case "complete targeting (2)" in Table 3 with the initial renormalized variances and dynamically reshaped covariances C3 is displayed on Fig. 8.

Figs. 7a, b show the structure of the σ_θ field at day 8, with initial conditions C1. The overall pattern is characteristic of dynamical error growth: maximum values are found along the frontal strips at both 0 m and 8000 m. The relative reduction observed on σ_θ is quite small, at about 20%. When the targeting is less efficient (smaller tracks or less observations), this reduction decreases even more to about 15%.

Figs. 8a, b show σ_θ at day 8, with initial conditions C3. Although the overall shape of the fields is similar to the previous case, maximum values are now drastically reduced: at 0 m, instead of 8–10 K on Fig. 7a, we have 6–7 K on Fig. 8a. At the tropopause, maxima reach about 5 K on Fig. 8b, versus about 7 K on Fig. 7b.

As a consequence, observations do have a strong impact but only with initial non-uniform, non-isotropic variances-covariances. In Table 2, it is seen that the analysis with complete targeting

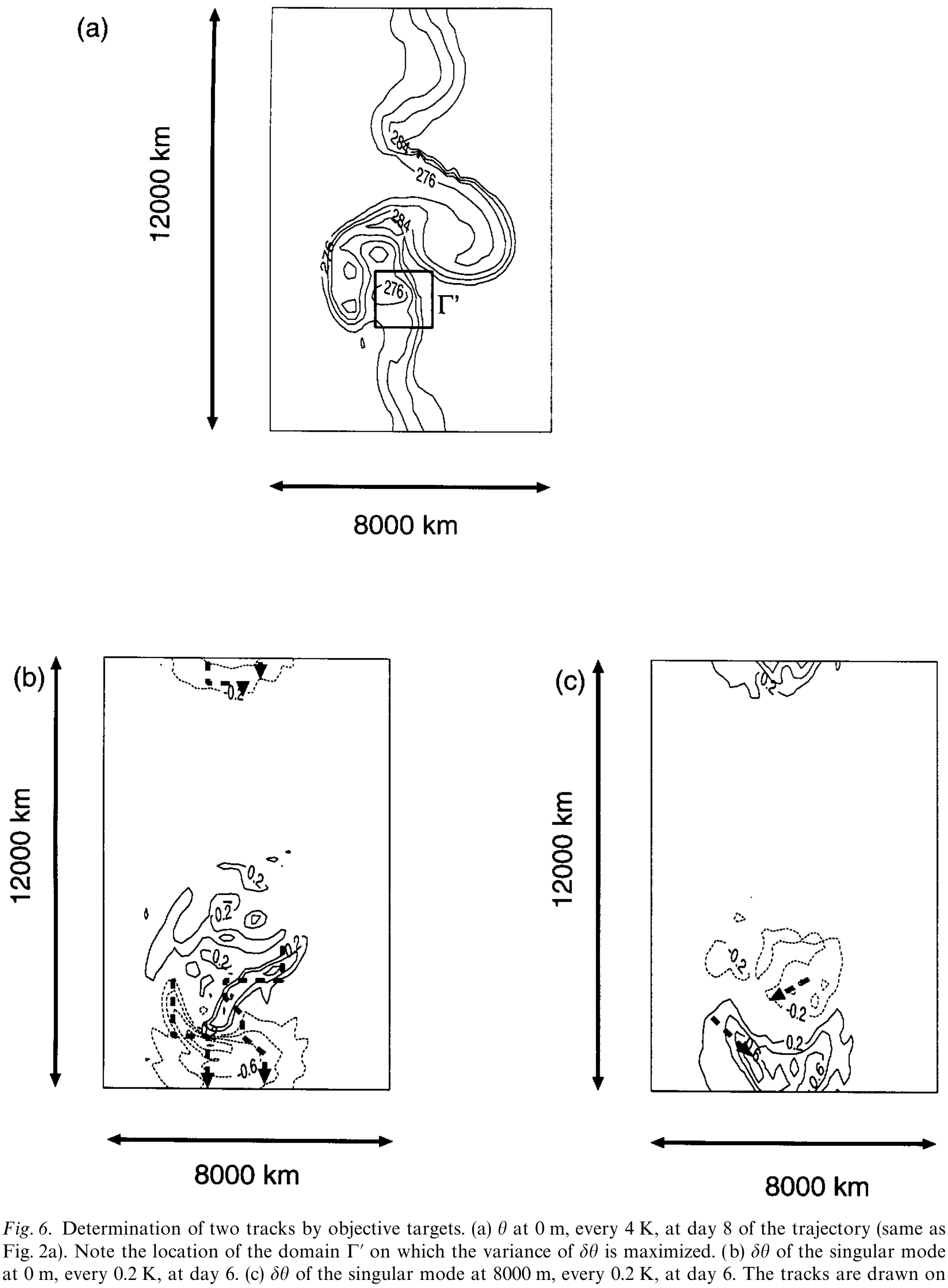

Fig. 6. Determination of two tracks by objective targets. (a) θ at 0 m, every 4 K, at day 8 of the trajectory (same as Fig. 2a). Note the location of the domain Γ' on which the variance of $\delta\theta$ is maximized. (b) $\delta\theta$ of the singular mode at 0 m, every 0.2 K, at day 6. (c) $\delta\theta$ of the singular mode at 8000 m, every 0.2 K, at day 6. The tracks are drawn on (b) and (c) with the dotted arrows.

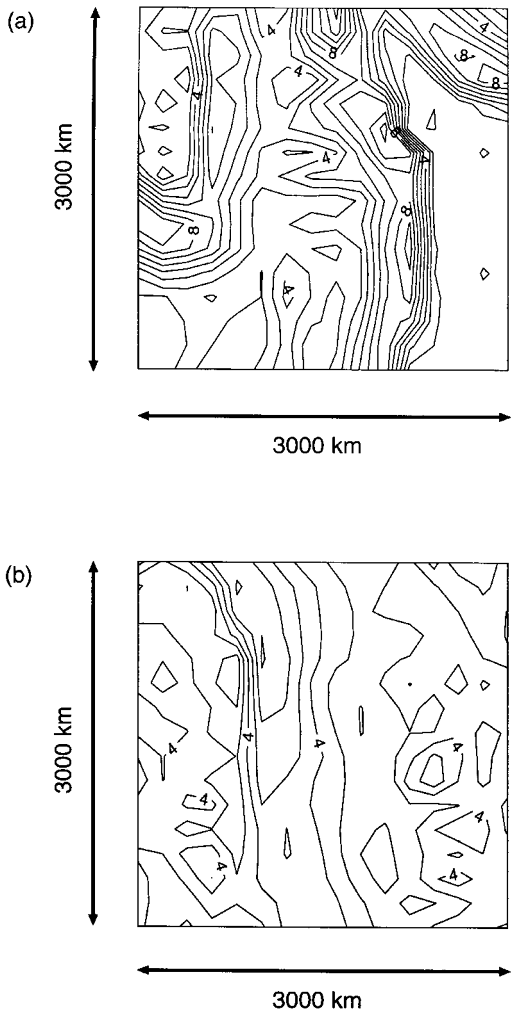

Fig. 7. Root mean square error σ_θ on potential temperature at day 8, every 1 K, for the case of a data supply every 15 min along the paths shown on Fig. 6b. (a) 0 m (b) 8000 m. Initial variances are uniform, and covariances are isotropic. The field is displayed in the subdomain Γ defined on Fig. 2.

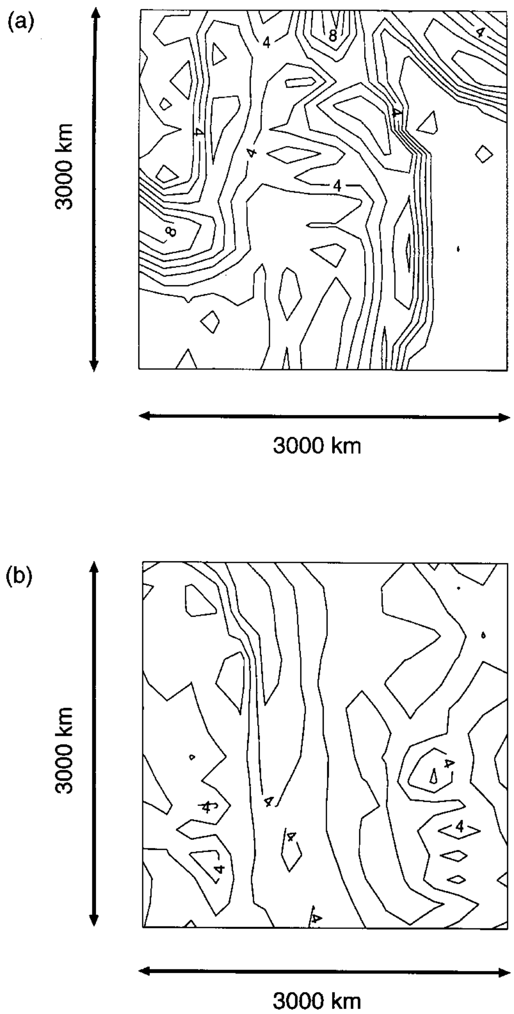

Fig. 8. Root mean square error σ_θ on potential temperature at day 8, every 1 K, for the case of a data supply every 15 min along the paths shown on Fig. 6b. (a) 0 m (b) 8000 m. Initial variances are renormalized, while the covariances have dynamically adapted structures (non-uniform). The field is displayed in the subdomain Γ defined on Fig. 2.

provides a reduction of more than 50% at day 8, which is a very "good" result, compared to the other IOSS. This figure is however sensitive to the quality of the targeting: limited paths provide only reductions of about 30 to 40%.

Anyhow, the net reduction shows the same behaviour with increased initial background errors (see in Table 3 the cases with initial σ_Θ set to 2 K and 4 K): with isotropic correlations, the decrease is of about 30%, while it reaches almost 60% with the dynamically fitted correlations. In accordance to this latter finding, a decreased observation RMS value (case with $\omega = 0.5$ K in Table 3) also gives a 60% net reduction with dynamical correlations. Only when the observation error becomes too large (case with $\omega = 2$ K in Table 3), does the impact on the analysis decrease.

Finally, the following results are emphasized.

- With our crude model resolution (200 km), the impact of the observations on the analysis has quite a large horizontal extent. This probably explains why the case with one orthogonal cross-frontal track produces a 45% reduction with non-uniform initial variances, though the number of soundings is very small (7).
- There is also an effect due to the distance between the track and the region of interest Γ. Thus, larger reductions in σ_θ are usually observed when the track is close to the Γ-domain (which is the case with the orthogonal transect and the downstream targeting, compared to the upstream targeting, for example).
- Surface observations alone give poor results, though the complete targeting track is used. This proves that error reduction is best achieved when the analysis modifies the RMS error at both boundaries at the same time.
- As shown previously, significant error reductions are obtained with the initial, dynamically reshaped correlations from the 12 h integration (conditions C2 and C3). Thus, the initial condition on the covariance matrix plays an important role, and this point is further addressed in the concluding discussion, section 6.
- The impact of this targeting strategy is found to be quite robust when the weight given to the observations is increased, compared to the initial background. In particular, this robustness shows that the results displayed in Table 2 hold for similar observation and background error variances in geostrophic space or, roughly speaking, for observation variances less than a quarter of the background variances in physical space. On the contrary, an increase of the observation error variance by a factor of four damps the positive impact of the dynamically fitted correlations in the analysis.

6. Discussion

Concerning the impact of non-permanent, widespread data, we observe frequently that the RMS values at day 8 are smaller with the dynamically reshaped, *non-renormalized* variances than with the uniform ones. On the contrary, at day 6, the former variances had larger values than the latter (see their description in Subsection 3.2). This is for example the case for the complete targeting with two tracks (see case "complete targeting (2)" in Table 2).

Therefore, the net reduction of absolute σ_θ values is much stronger with the dynamically tuned covariances C2. The result also holds for complete targeting and renormalized variances C3 (first two lines in Table 3). In this latter case, the day 6 variances have the same amplitude than for the uniform and isotropic case. Thus, the very efficient net reduction in σ_θ is not due to the different initial error variances, but to the different correlation functions that are used.

To be specific, the flow dependent correlations allow for a better damping of error growth than the initial isotropic correlations. This shows that a significant improvement can be obtained in the analysis and in subsequent forecasts, when dynamically consistent covariances are chosen instead of the conventional analytical formulations. It also underlines the potential superiority of four-dimensional variational assimilation, where error covariances are implicit but dynamically consistent, compared to three-dimensional variational assimilation, where the error correlations still are prescribed analytically.

As far as the objective targeting is concerned, the following remarks are made.

- The simulations with one cross-frontal track and with the complete target give consistent and rather similar results.
- Simulations based on targeting only produce a significant improvement in error reduction when the initial covariances are flow dependent. This implies that the targeting strategies can be efficient only when dynamically consistent 2nd-order error statistics are constructed.
- Since the sensitivity area is very broad, a great number of tracks pass through this area, even some paths that are not a priori chosen with respect to an objective criterion. Anyway, the sensitivity fields can be used as an indication for the overall properties of the dominating linear modes: phase speeds, wavelengths, orientation, vertical structure. This information can then be used to determine efficient targeted paths in space and time.

These conclusions are found to be robust, and hold when the ratio of observation to background error variance is decreased by a factor of 4, thus forcing a stronger fit towards the observations.

Note that, for the mesoscale, both the error structures and the sensitivity fields will become more complex. Computations with a refined grid in the SG model have shown that the variances basically adapt themselves to the main mesoscale dynamical features, such as areas of strong vorticity. Therefore, the main difficulty is to obtain a computationally tractable description of the error covariance matrix at mesoscale. Thus, the validity of our results in a mesoscale assimilation system is not straightforward. At least, it seems evident that the targeting approach will become more complex, since the number of degrees of freedom in the flow will be larger than in the present, synoptic scale study.

This work concentrates deliberately on data-sparse systems, and it is foreseeable that the usage of more and more observations (with the same quality) will decrease the difference between the final analysis with C1 or C3-type of covariances. However, when going to operational systems, this increase of observations merely underlines the potential need for high-density observation networks. Note also that in our SG model, the addition of extra observations can quickly lead to dynamical inconsistencies, due to the model simplifications. In that case, one should then also take into account the model errors or the error of representativeness of the observations, if the assumption of a perfect model is to be kept.

The singular vector approach used in this study gives the sensitivity to the growth of the forecast variance as measured with the $\langle .,. \rangle$-norm of Section 5. At this stage, the variance of interest is that of the F-function, without an explicit reference to the model state itself. For the more general problem of reducing the forecast errors on the model state, it is interesting to study the eigenvectors of the operator $L(LP_k^a)^*$ that is involved in eq. (7). This gives actually the set of the so-called "empirical orthogonal functions" (EOF). Such a task is possible with a low-dimensional model like the SG model, but this would be impossible with present computer resources in an operational model. At this stage, one should at first simplify the previous operator, for example by retaining only a set of dominating EOFs. This technique is used by Houtekamer (1995) in a three-level quasi-geostrophic model. In particular, Houtekamer shows that nonlinear effects become important after some 4.5 days. The dominating EOFs are typically computed over a 1.5-day interval, with 32 modes retained. An alternative approach is presented in Palmer et al. (1998). These authors compare the spectrum of several singular modes with an estimated spectrum of the analysis error, and find the energy-related singular vector to be the best approximation of the error field. As a consequence, they claim that the energy-related metric fits best to the searched "analysis error covariance metric", which is measured with the P_k^a. The first singular vectors to this metric then give the dominating features in the forecast error covariance matrix $P_{k+1}^f = L(LP_k^a)^*$.

The IOSS with a permanent data supply give significant error reductions, regardless of the initial covariance field. However, measurements are best performed all over the period of interest (here, 48 h). The effect-at-a-distance, due to advective and propagative phenomena, allows for a significant impact some 2000 km downstream of the source locations. The robustness of the results with respect to the initial conditions might show that this kind of data source is useful in an operational context, by providing error damping regardless of the way the correlations are prescribed in the operational analysis. This could be verified in the framework of an operational, calibrated data assimilation system in the ongoing work of the FASTEX experiment. Note also that a 24-h analysis cycle, followed by 24-h dynamical growth, with two fixed data sources, provides an error reduction that is similar to the cases with only one source, or the cases with limited targeted paths. This suggests that the fixed sources are only efficient if their observations are taken close to the validating time, and that a limited targeted data supply, over a shorter time, might be just as efficient, provided that the analysis uses error statistics that are fitted to the flow.

Furthermore, we stress the importance of the source locations. They have to be close to the large scale frontal structures. The SG model gives a good description of adiabatic, baroclinic development by means of wave interactions between both boundaries. In this context, it is found useful to have both an observation at the surface front and at the jet level.

All these concluding remarks are qualitative with respect to operationally implemented data assimilation systems. Our numerical, quantitative results (displayed in Tables 1–3) allow for general qualitative conclusions that should still hold in more realistic systems for the synoptic-scale features. Thus, we anticipate the potential strength of 4D-VAR-like data assimilation coupled with objectively targeted observations. Note finally that the sensitivity to the observation error variance suggests that there might be a critical value for the ratio of observation to background RMS errors ω/σ_θ above which any targeted approach would be useless, due to a lack of precision in the measurements.

7. Acknowledgements

The work benefited from discussions with Pierre Bernardet and Gérald Desroziers. Chris Snyder contributed to some improvements on the numerical model. Claude Fischer is also grateful to the École Nationale de la Météorologie, which allowed for a longer stay at the Centre National de Recherches Météorologiques, both institutes being part of Météo-France.

8. Appendix

On the true conversion from geostrophic to physical error covariances

As pointed out by Bernardet (personal communication), the proper conversion from geostrophic space error covariances to physical space ones requires to take into account the uncertainty of the coordinate change itself (relation (3)). Indeed, since an uncertainty on the velocity field is prescribed, the positions in physical space, given the positions and error statistics in geostrophic space, are not known precisely. Algebraically, this uncertainty introduces the need for rescaling the error covariances. Only if this rescaling is performed, does the Kalman filter behave consistently with the semi-geostrophic nature of the model. Otherwise, we might underestimate the error variances (as shown below), just as the quasi-geostrophic models underestimate local gradients, so that our present Kalman filter might be called a "quasi-geostrophic" one. For instance, Fischer (1997) develops the conversions for the semi-geostrophic model. In the following, uppercase letters stand for geostrophic space fields and lower case letters for physical space quantities. Then, the conversion from the geostrophic error covariance matrix to the physical space one reads, for wind, geopotential and potential temperature respectively:

$$P_{v,u}(x_1, y_1, x_2, y_2) = E\left\{\begin{pmatrix} v''_{g1} \\ u''_{g1} \end{pmatrix} ((v''_{g2})^t, (u''_{g2})^t)\right\}, \tag{19}$$

with $P_{v,u}(x_1, y_1, x_2, y_2)$ the square matrix of the wind error covariances between 2 points in physical space. The double quote stands for an individual bias and $E\{\ \}$ is the statistical mean.

$$P_{v,u} = TC^{-1}_{X_1,Y_1} TP_{V,U} T(C^{-1}_{X_2,Y_2})^t T, \tag{20}$$

$$P_\phi = P_\Phi, \tag{21}$$

$$\begin{aligned} P_\theta = {} & \left(\frac{\theta_0}{g}\right)^2 \left(\frac{\partial V_g}{\partial Z}, \frac{\partial U_g}{\partial Z}\right)_1 T(C^{-1}_{X_1 Y_1})^t TP_{V,U} TC^{-1}_{X_2,Y_2} T \\ & \times \begin{pmatrix} \dfrac{\partial V_g^t}{\partial Z} \\ \dfrac{\partial U_g^t}{\partial Z} \end{pmatrix}_2 + \frac{\theta_0}{g}\left(\frac{\partial V_g}{\partial Z}, \frac{\partial U_g}{\partial Z}\right)_1 T(C^{-1}_{X_1,Y_1})^t TP_{V,U/\Theta} \\ & + P_{\Theta/V,U} TC^{-1}_{X_2,Y_2} T \begin{pmatrix} \dfrac{\partial V_g^t}{\partial Z} \\ \dfrac{\partial U_g^t}{\partial Z} \end{pmatrix}_2 \frac{\theta_0}{g} + P_\Theta, \end{aligned} \tag{22}$$

with the multivariate covariances:

$$\begin{aligned} P_{V,U/\Theta} &= E\left\{\begin{pmatrix} V''_{g1} \\ U''_{g1} \end{pmatrix} (\Theta''_2)^t\right\}, \\ P_{\Theta/V,U} &= E\{\Theta''_1((V''_{g2})^t, (U''_{g2})^2)\} \end{aligned} \tag{23}$$

and the horizontal part of the jacobian matrix in geostrophic space C and the operator T:

$$\begin{aligned} C_{X,Y} &= \begin{pmatrix} 1 - \dfrac{1}{f}\dfrac{\partial V_g}{\partial X} & -\dfrac{1}{f}\dfrac{\partial V_g}{\partial Y} \\ \dfrac{1}{f}\dfrac{\partial U_g}{\partial X} & 1 + \dfrac{1}{f}\dfrac{\partial U_g}{\partial Y} \end{pmatrix}, \\ T &= \begin{pmatrix} 1 & 0 \\ 0 & -1 \end{pmatrix}. \end{aligned} \tag{24}$$

To illustrate the impact of these conversions, we consider the simplified case of a single point and two-dimensional dynamics (so that $U_g = 0$ and Y-derivatives cancel). The wind error variance is then simply multiplied by the square of the jacobian J_X (relation (4)):

$$\sigma_v^2 = J_X^2 \sigma_V^2. \tag{25}$$

The geopotential error is identical to the geostrophic potential error, from geostrophic to physical space:

$$\sigma_\phi = \sigma_\Phi . \tag{26}$$

For potential temperature, the relationship is more complicated. In our simplified example, we neglect the two terms that involve the multivariate covariances, and thus the conversion reads:

$$\sigma_\theta^2 \approx \sigma_\Theta^2 + \left(\frac{\theta_0}{g}\frac{\partial V_g}{\partial Z} J_X\right)^2 \sigma_V^2 . \tag{27}$$

With typical values taken from our experimental set, we obtain:

$$\frac{\theta_0}{g} \approx 30\mathrm{SU}, \qquad \frac{\partial V_g}{\partial Z} \approx 5 \cdot 10^{-3}\ \mathrm{SU}, \qquad J_X \leqslant 10, \qquad \sigma_V^2 \approx 1\ \mathrm{SU} \tag{29}$$

$$\Rightarrow \sigma_\theta^2 \leqslant k\sigma_\Theta^2 \qquad \text{with } k \in [1, 10] \tag{29}$$

in standard units SU. Thus, the potential temperature variances are corrected by an additional term, which comes from the thermal wind relationship in the coordinate change.

In our experiences, the conversion therefore implies changes on the wind variances of about 2 orders of magnitude at most. On the opposite, temperature variances are modified by only one order of magnitude at the most, and geopotential variances are left untouched. As a consequence, the weight of the guess field is too high in the present Kalman filter, since our procedure underestimates the physical space variances. However, it is possible to sketch the behaviour of the complete "semi-geostrophic" Kalman filter with for instance the same values for observation and background error variances by choosing larger initial background errors in our "quasi-geostrophic" filter, with a multiplication typically between 1 and 10.

REFERENCES

Bergot, T., S. Malardel and A. Joly. 1996. Sensitivity and singular vectors calculation in the operational context of FASTEX. In: *7th Conf. on Mesoscale Proc.*, pp. 366–368. Reading, UK.

Bouttier, F. 1993. The dynamics of error covariances in a barotropic model. *Tellus*. **45A**, 408–423.

Budgell, W. 1986. Nonlinear data assimilation for shallow water equations in branched channels. *J. Geoph. Res.* **91 C9**, 10,633–10,644.

Dee, D. P. 1995. On-line estimation of error covariance parameters for atmospheric data assimilation. *Mon. Wea. Rev.* **123**, 1128–1145.

Eady, E. 1949. Long waves and cyclone waves. *Tellus*, **1**, 33–52.

Farrell, B. F. 1988. Optimal excitation of neutral Rossby waves. *J. Atmos. Sci.* **45**, 163–172.

Farrell, B. F. 1990. Small error dynamics and the predictability of atmospheric flows. *J. Atmos. Sci.* **47**, 2409–2416.

Fischer, C. 1997. *Estimation d'erreurs de prévision et d'analyse dans un modèle semi-géostrophique à l'aide d'un filtre de Kalman.* Technical report, Météo-France/CNRM. Note de centre GMME no. 48.

Fischer, C. 1998. Linear amplification and error growth in the 2D Eady problem with uniform potential vorticity. *J. Atmos. Sci.*, in press.

Gandin, L. 1963. *Objective analysis of meteorological fields.* Israel program for scientific translations, 242 pp., translated from Russian, 1965 edition.

Gauthier, P., P. Courtier and P. Moll, 1993. Assimilation of simulated wind lidar data with a Kalman filter. *Mon. Wea. Rev.* **121**, 1803–1820.

Ghil, M. 1989. Meteorological data assimilation for oceanographers. Part I: description and theoretical framework. *Dyn. Atmos. Oc.* **13**, 171–218.

Ghil, M., S. Cohn, T. J. K. Bube, and E. Isaacson. 1981. Applications of estimation theory to numerical weather predictions. In: *Dynamic meteorology: data assimilation methods*, L. Bengtsson, M. Ghil, E. Källén (eds.), New York: Springer Verlag, pp. 139–224.

Hoskins, B. 1975. The geostrophic momentum approximation and the semi-geostrophic equations. *J. Atmos. Sci.* **32**, 233–242.

Hoskins, B. J. and F. P. Bretherton, 1972. Atmospheric frontogenesis models: mathematical formulation and solution. *J. Atmos. Sci.* **29**, 11–36.

Houtekamer, P. 1995. The construction of optimal perturbations. *Mon. Wea. Rev.* **123**, 2888–2898.

Joly, A. 1995. The stability of steady fronts and the adjoint method: nonmodal frontal waves. *J. Atmos. Sci.* **52**, 3081–3108.

Joly, A. and A. J. Thorpe. 1991. The stability of time-dependent flows: an application to fronts in developing baroclinic waves. *J. Atmos. Sci.* **48**, 163–182.

Kalman, R. 1960. A new approach to linear filtering and prediction problems. *Trans. ASME* **82D**, 35–45.

Kalman, R. and R. Bucy. 1961. New results in linear filtering and prediction theory. *Trans. ASME* **83D**, 95–108.

Lacarra, J.-F. and O. Talagrand, 1988. Short-range evolution of small perturbations in a barotropic model. *Tellus* **40A**, 81–95.

Langland, R. H. and G. D. Rohany. 1996. Adjoint-based targeting of observations for FASTEX cyclones. in:

Seventh Conf. on Mesoscale Proc., pp. 369–371. Reading, U.K.

Menard, R. and R. Daley, 1996. The application of Kalman smoother theory to the estimation of 4DVAR error statistics. *Tellus* **48A**, 221–237.

Palmer, T. N., R. Gelaro, J. Barkmeijer and R. Buizza. 1998. Singular vectors, metrics and adaptive observations. *J. Atmos. Sci.* **55**, 633–653.

Rabier, F., E. Klinker, P. Courtier and A. Hollingsworth. 1996. Sensitivity of forecast errors to initial conditions. *Quart. J. Roy. Meteor. Soc.* **122**, 121–150.

Rutherford, I. 1972. Data assimilation by statistical interpolation of forecast error fields. *J. Atmos. Sci.* **29**, 809–815.

Snyder, C. 1996. Summary of an informal workshop on adaptive observations and FASTEX. *Bull. Am. Meteor. Soc.* **77**, 953–961 (meeting summary).